J. Fluid Mech. (2016), *vol.* 801, *pp.* 65–90.
doi:10.1017/jfm.2016.412

Propagation of viscous currents on a porous substrate with finite capillary entry pressure

Roiy Sayag[1,2,†] **and Jerome A. Neufeld**[3,4,5]

[1]Department of Environmental Physics, Blaustein Institutes for Desert Research, Ben-Gurion University of the Negev, Sede Boqer Campus, 8499000, Israel

[2]Department of Mechanical Engineering, Ben-Gurion University of the Negev, Beer-Sheva 8410501, Israel

[3]BP Institute, University of Cambridge, Cambridge CB3 0EZ, UK

[4]Department of Earth Sciences, Bullard laboratories, University of Cambridge, Cambridge CB3 0EZ, UK

[5]Department of Applied Mathematics and Theoretical Physics, University of Cambridge, Cambridge CB3 0WA, UK

(Received 15 November 2015; revised 3 May 2016; accepted 13 June 2016; first published online 19 July 2016)

We study the propagation of viscous gravity currents over a thin porous substrate with finite capillary entry pressure. Near the origin, where the current is deep, propagation of the current coincides with leakage through the substrate. Near the nose of the current, where the current is thin and the fluid pressure is below the capillary entry pressure, drainage is absent. Consequently the flow can be characterised by the evolution of drainage and fluid fronts. We analyse this flow using numerical and analytical techniques combined with laboratory-scale experiments. At early times, we find that the position of both fronts evolve as $t^{1/2}$, similar to an axisymmetric gravity current on an impermeable substrate. At later times, the growing effect of drainage inhibits spreading, causing the drainage front to logarithmically approach a steady position. In contrast, the asymptotic propagation of the fluid front is quasi-self-similar, having identical structure to the solution of gravity currents on an impermeable substrate, only with slowly varying fluid flux. We benchmark these theoretical results with laboratory experiments that are consistent with our modelling assumption, but that also highlight the detailed dynamics of drainage inhibited by finite capillary pressure.

Key words: gravity currents, interfacial flows (free surface), porous media

1. Introduction

Gravity currents are thin, horizontal flows that are driven by the buoyancy difference between an intruding and an ambient fluid, and occur in a wide range of natural and industrial settings (Simpson 1999; Huppert 2006). When gravity currents propagate over a porous substrate, some of the mass in the current can leak into the substrate, slowing down and sometimes inhibiting the propagation of the current. Such flow

† Email address for correspondence: roiy@bgu.ac.il

configurations could occur, for example, when a breaking wave interacts with the sediment on continental shelf (Boczar-Karakiewicz, Bona & Pelchat 1991), during a spill of contaminating liquids from containers surrounded by gravel beds (Grobelbauer, Fannelop & Britter 1993), following the sequestration of CO_2 in deep aquifers (Huppert & Neufeld 2014), when glacial melt-water reaches the interface between the base of the ice and a porous bed (Das *et al.* 2008) or when honey spreads over a slice of bread.

Viscous gravity currents on impermeable, flat substrates are known to have self-similar solutions (Huppert 1982), with the fluid front propagating as $t^{1/2}$ when the fluid is discharged axisymmetrically at constant rate. Viscous currents on permeable substrates involve two moving fronts, a fluid front that propagates over the substrate, and a drainage front that demarcates the leading position where fluid percolates into the substrate (Thomas, Marino & Linden 1998; Pritchard, Woods & Hogg 2001; Spannuth *et al.* 2009). Where such currents are fed by a constant flux, leakage through the substrate grows as the contact area of the current with the substrate increases until eventually leakage balances the influx allowing the current to reach a steady state (Spannuth *et al.* 2009), in contrast with the case for gravity currents on an impermeable substrate.

The leakage of gravity currents that propagate over saturated porous substrates typically involves a low pore Reynolds number and therefore can be modelled with Darcy's law. The case of a thin porous substrate may be modelled using only a pressure gradient component acting over the constant thickness of the substrate (Thomas *et al.* 1998; Ungarish & Huppert 2000; Pritchard *et al.* 2001; Marino & Thomas 2002). In the case of deep porous media of both inertial and viscous currents, percolation laws typically account for gravity in addition to a pressure gradient component that is applied over the evolving depth of the draining fluid in the porous medium (Acton, Huppert & Worster 2001; Thomas, Marino & Linden 2004; Spannuth *et al.* 2009).

The position of the fluid and drainage fronts coincide if leakage begins immediately once fluid contacts the substrate. In contrast, the presence of a finite capillary entry pressure can limit the migration of the propagating fluid into the porous substrate, resulting in the fluid and the drainage fronts propagating at different rates. Interfacial tension acting between the invading liquid and the ambient pore fluid restricts the propagating fluid from passing through pore throats (Bear 1988). The magnitude of the capillary entry pressure depends on the interfacial tension between the two fluid phases and on the pore size. The presence of a capillary entry pressure requires the fluid in the current to have a minimum overpressure before it can overcome the capillary entry pressure and drain through the surface layer of the substrate.

The impact of capillary pressure on percolation has been previously studied in several contexts. Viscous spreading of a liquid drop on a porous substrate can involve rich and complex structure, and accounting for the movement of contact lines within the pores can become important (Davis & Hocking 2000, 1999). In the case of a gravity current propagating within a porous layer along a low-permeability barrier (Woods & Farcas 2009) the impact of finite capillary entry pressure has led to the partitioning of the current into several regions, including a steady region in which drainage was active, an intermediate region in which the depth of the surface current is equal to the capillary depth and a region in which the propagation of the surface current is similar to a gravity current in a porous layer on impermeable surface (Huppert & Woods 1995).

In the present study we consider the propagation of an axisymmetric viscous gravity current over a porous substrate with conditional percolation set by a capillary entry

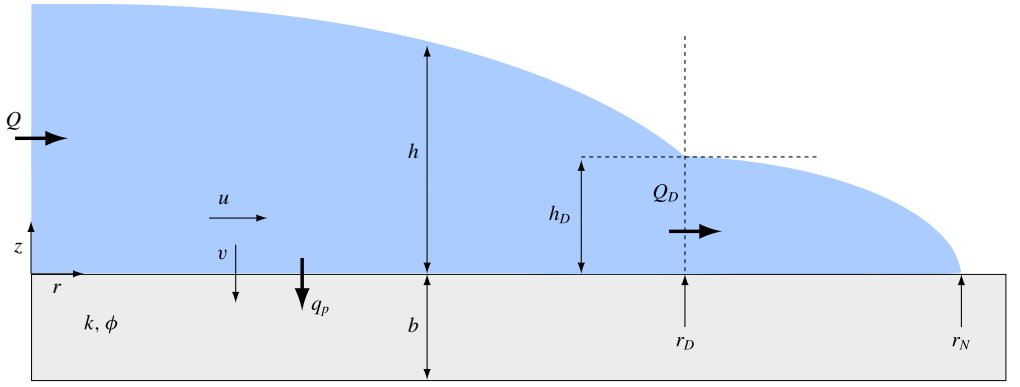

FIGURE 1. (Colour online) Schematic diagram of a gravity current on a porous substrate with finite entry pressure. The current has a thick inner region ($r \leqslant r_D(t)$) in which the drainage through the substrate is $q_p > 0$ and a shallower outer region ($r_D(t) < r \leqslant r_N(t)$) in which the fluid depth in under the critical capillary depth.

pressure. We investigate the evolution of such currents over a relatively thin substrate using theoretical and numerical analysis, combined with laboratory experiments. Specifically, we develop a physical model which accounts for the explicit evolution of the free surface and of the two fronts. In addition, we validate the numerical results with early-time and late-time asymptotic solutions and develop semi-analytical solutions for the evolution of the fronts and the free surface. The results of our theoretical model are tested in the laboratory using an experimentally determined drainage law which phenomenologically captures the behaviour of our theoretical model. The results of the combined theoretical and experimental study are then discussed.

2. Theoretical analysis

2.1. *Physical model*

We consider a fluid of kinematic viscosity ν and density ρ that spreads axisymmetrically over a flat, porous substrate of permeability k, porosity ϕ and thickness b (see figure 1). For such long, thin viscous currents, when the leakage rate is small, the pressure within the current is nearly hydrostatic. When the viscous current extends over a distance much greater than the capillary length,

$$\ell_c = \frac{\gamma}{\rho g}, \tag{2.1}$$

where γ is the surface tension and g the gravitational acceleration, we may neglect capillary forces on the top surface of the current. The upper surface of the current is stress free and, when the porosity and permeability of the substrate are small, we may apply a no-slip condition at the porous interface, to leading order. The radial velocity, driven by gradient in the hydrostatic pressure, is

$$u = -\frac{g}{\nu}\frac{\partial h}{\partial r}\left(hz - \frac{z^2}{2}\right), \tag{2.2}$$

where r, z are respectively the radial and vertical coordinates, and $h(r, t)$ is the fluid thickness. The horizontal flux, given by the depth-integrated radial velocity, is

$$q = \int_0^h u \, \mathrm{d}z = -\frac{g}{3\nu} h^3 \frac{\partial h}{\partial r}. \tag{2.3}$$

Local conservation of mass implies that

$$\frac{\partial h}{\partial t} + \frac{1}{r}\frac{\partial}{\partial r}(rq) = -v_p, \tag{2.4}$$

where v_p is the vertical leakage flux due to drainage through the porous substrate.

When the substrate is initially dry, capillary forces acting on the small length scale of the pore diameter d_p act to inhibit entry of the fluid into the substrate. To initiate the flow v_p in the substrate, the fluid pressure must exceed the capillary entry pressure. The fluid pressure is predominately hydrostatic when the length of the surface current is much larger than its depth, and hence the fluid must reach a critical depth to initiate drainage, which we denote as the capillary depth h_D (Bear 1988). The leakage flow is then driven by the overpressure of the fluid above the substrate. Where the depth of the propagating fluid is less than the capillary depth, interfacial tension inhibits flow into the substrate. The control on drainage exerted by the capillary entry pressure results in a discontinuous boundary condition on the dynamics of the propagating current,

$$v_p = \begin{cases} \phi \dfrac{kg}{\nu}\left(\dfrac{h}{b} + 1\right), & h \geqslant h_D, \\ 0, & h < h_D, \end{cases} \tag{2.5}$$

where

$$h_D = \frac{4\gamma \cos\theta}{\rho g d_p} \tag{2.6}$$

is the critical depth of the surface current corresponding to the critical capillary entry pressure, with contact angle θ. Here we have modelled the percolation velocity using Darcy's law, with fluid flow being driven by both the pressure gradient across the substrate and the weight of the fluid. This expression for the leakage is valid once the fluid fills the entire depth of the porous layer, namely, on time scales longer than b/v_p. For thin substrates, the time scale for the viscous propagation of the fluid front through the substrate is shorter; and so we neglect to model the evolving fluid front within the porous layer, as has been done previously for deep porous media (e.g. Davis & Hocking 2000; Spannuth *et al.* 2009). Substituting (2.3), (2.5) in (2.4), the evolution of the axisymmetric current may be described by

$$\frac{\partial h}{\partial t} - \frac{g}{3\nu}\frac{1}{r}\frac{\partial}{\partial r}\left(rh^3\frac{\partial h}{\partial r}\right) = \begin{cases} -\phi \dfrac{kg}{\nu}\left(\dfrac{h}{b} + 1\right), & r < r_D, \\ 0, & r_D \leqslant r \leqslant r_N, \end{cases} \tag{2.7a}$$

where the drainage front $r = r_D(t)$ continuously adjusts to satisfy the condition that $h(r_D, t) = h_D$ and $r = r_N(t)$ is the fluid front where $h(r_N, t) = 0$. The four boundary conditions necessary to fully specify the problem are

$$2\pi r q = Q \quad \text{as } r \to 0, \tag{2.7b}$$

$$h = h_D \quad \text{at } r = r_D, \tag{2.7c}$$

$$2\pi r q = 0 \quad \text{at } r = r_N, \tag{2.7d}$$

$$h = 0 \quad \text{at } r = r_N. \tag{2.7e}$$

These conditions specify the input flux Q at the origin, the critical depth set by the capillary entry pressure at the edge of the drainage region and conditions of zero flux through and zero height at the nose of the current, respectively. The boundary condition (2.7*d*) can be derived from a statement of global mass conservation

$$2\pi \int_0^{r_N} rh \,\mathrm{d}r + 2\pi \int_0^{r_D} \int_0^t v_p r \,\mathrm{d}t \,\mathrm{d}r = Qt, \tag{2.8}$$

by differentiating (2.8) with respect to time, and using (2.7). We note that continuity of both h and the local flux $q \propto \partial h/\partial r$ at $r = r_D$ is implicit in (2.7).

2.2. *Dimensionless quantities*

Unlike the flow of viscous fluids over an impermeable surface, a unique vertical length scale exists in the problem due to the capillary forces acting within the pore space as represented by the critical depth. We therefore non-dimensionalise (2.7) by scaling depth by the drainage height, the radial extent by the steady-state balance between horizontal flux and leakage and time by the characteristic time to reach the steady state,

$$\hat{h} = h/h_D, \quad \hat{r} = r \Bigg/ \sqrt{\frac{h_D^4}{3\phi k}}, \quad \hat{t} = t \Bigg/ \left(\frac{\nu h_D}{\phi k g}\right). \tag{2.9a–c}$$

Therefore, the dimensionless equations (hats removed) are

$$\frac{\partial h}{\partial t} - \frac{1}{r}\frac{\partial}{\partial r}\left(rh^3 \frac{\partial h}{\partial r}\right) = \begin{cases} -(\lambda h + 1), & r < r_D, \\ 0, & r_D \leqslant r \leqslant r_N, \end{cases} \tag{2.10a}$$

with the boundary conditions,

$$rh^3 \frac{\partial h}{\partial r} = -\mathscr{Q} \quad \text{as } r \to 0, \tag{2.10b}$$

$$h = 1 \quad \text{at } r = r_D, \tag{2.10c}$$

$$rh^3 \frac{\partial h}{\partial r} = 0 \quad \text{at } r = r_N, \tag{2.10d}$$

$$h = 0 \quad \text{at } r = r_N, \tag{2.10e}$$

where the system is now a function of two non-dimensional quantities,

$$\lambda = \frac{h_D}{b}, \quad \mathscr{Q} = \frac{3\nu Q}{2\pi g h_D^4}, \tag{2.11a,b}$$

that characterise the critical entry depth and the input flux respectively.

2.3. *Numerical solution of the full evolution*

The full temporal evolution of the flow is found numerically by integrating (2.10), which we do by mapping the percolating and non-percolating domains on to a fixed

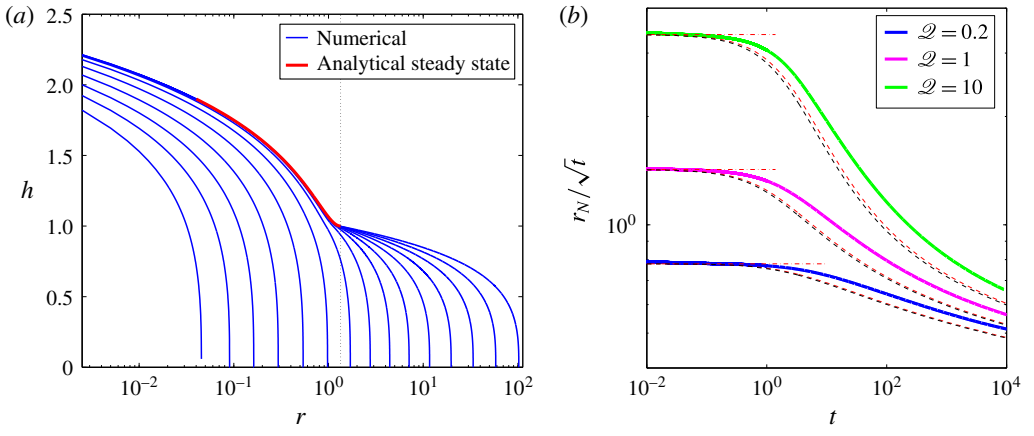

FIGURE 2. (Colour online) (*a*) Numerical solution of the evolution of the current for $\lambda = 0.1$, $\mathscr{Q} = 1$, showing the evolution of the free surface (—— blue) starting at $t = 10^{-2}$ and ending at $t = 3.8 \times 10^4$. The temporal spreading of the profiles is uniform in the log(t) space. The steady-state solution of the drainage-active region in the limit $\mathscr{Q}_D = 0$ (2.17) is shown (—— red), where the position of the steady-state drainage front is marked by a vertical grid line. (*b*) Evolution of the fluid front r_N for $\lambda = 0.1$ and for $\mathscr{Q} = 0.2$, 1, 10, showing the full numerical solutions (thick curves), the asymptotic estimates of the early time evolution (– – –, red), and the asymptotic estimates of the late-time evolution (– – – – red) for the case $\lambda \ll 1$ and $\mathscr{Q} = 0$ and (– – – – black) for the finite λ and non-zero $\mathscr{Q}_D$ case, which are evaluated also at early time.

interval. Such mappings involve two additional evolution equations for the fronts

$$\dot{r}_D = -\left.\frac{\partial h/\partial t}{\partial h/\partial r}\right|_{r=r_D}, \tag{2.12a}$$

$$\dot{r}_N = \left.\frac{q}{h}\right|_{r=r_N}, \tag{2.12b}$$

which we obtain, respectively, by time differentiation of the boundary condition (2.10*c*) and by assuming that the surface front evolves kinematically. This approach also requires two additional boundary conditions that we explicitly write as

$$[\![h]\!] = [\![q]\!] = 0 \quad \text{at } r = r_D, \tag{2.13}$$

which correspond to continuity of thickness and flux at the interface. We solve the complete system simultaneously for the free surface and the position of the front in each domain (appendix A). We evaluate the quality of our numerical scheme by checking consistency of the case of no drainage with the self-similar solution of a gravity current on an impermeable substrate (Huppert 1982), which we also use as an initial condition. We have also confirmed consistency of the numerical solution with the analytical solutions of the fully prewetted substrate (appendix A) and of the late-time asymptotic flow in the permeable region (figure 2*a*).

The simulated evolution of the current is shown in figure 2. At early times ($t \ll 1$) drainage is confined to a small region ($r_D \ll 1$) and the horizontal flux across the drainage front $\mathscr{Q}_D$ is roughly equivalent to $\mathscr{Q}$. Therefore the impact of the drainage

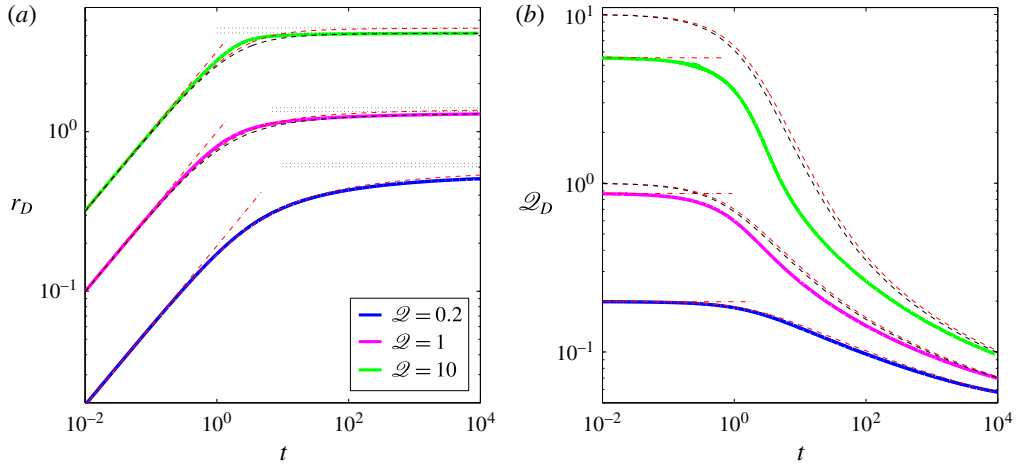

FIGURE 3. (Colour online) (*a*) Evolution of the drainage front r_D and (*b*) the evolution of the horizontal flux at the drainage front $\mathscr{Q}_D$ for $\lambda = 0.1$ and for $\mathscr{Q} = 0.2, 1, 10$, showing the full numerical solutions (thick curves), the asymptotic estimate of the early time evolution (– – –), the asymptotic estimates of the late-time evolution for $\lambda \ll 1$, $\mathscr{Q}_D = 0$ (– – – red) and for the finite λ and non-zero $\mathscr{Q}_D$ case (– – – black). For each of the three $\mathscr{Q}$ values in (*a*), two horizontal grid lines mark the two approximations of steady-state solutions to equations (2.16), the top being (2.17*b*).

on the current is negligible and the behaviour is, to leading order, that of a constant flux, viscous gravity current on an impermeable substrate (Huppert 1982), for which $r_N \sim r_D \sim t^{1/2}$ (figures 2*b*, 3*a*). When $t \gg 1$ the drainage front slows down and approaches a steady position in which the leakage flux nearly balances the input flux (figure 3*a*), while the fluid front advances again as $t^{1/2}$, albeit with a smaller prefactor that varies slowly in time, equivalent to a reduced input flux (figure 2*b*). In this regime, the flux across the drainage front becomes smaller than Q and decreases indefinitely (figure 3*b*). To obtain a more quantitative evaluation of the quality of the numerical simulation we investigate the asymptotic behaviour of the solutions in the following sections.

2.4. *Early-time evolution*

At early times ($r_N \ll 1$) the drainage front is small, $r_D \ll 1$, so that little fluid leaks from the current. In this limit we recover, to leading order, the self-similar spreading of an non-leaking current (Huppert 1982), in which the viscous gravity current has a self-similar form for the height and radial extent given by

$$h(r, t) = \xi_N^{2/3} (2\pi\mathscr{Q})^{1/4} \psi(y), \tag{2.14a}$$

$$r_N = \xi_N (2\pi\mathscr{Q})^{3/8} t^{1/2}, \tag{2.14b}$$

where $\xi = r(2\pi\mathscr{Q})^{-3/8} t^{-1/2}$, $y = \xi/\xi_N$ and $\xi_N = \xi(r = r_N) \approx 0.715$ together with $\psi(z)$ describe the self-similar solution in the absence of leakage (Huppert 1982). The position of the drainage front is given by

$$r_D = y_D r_N, \tag{2.15a}$$

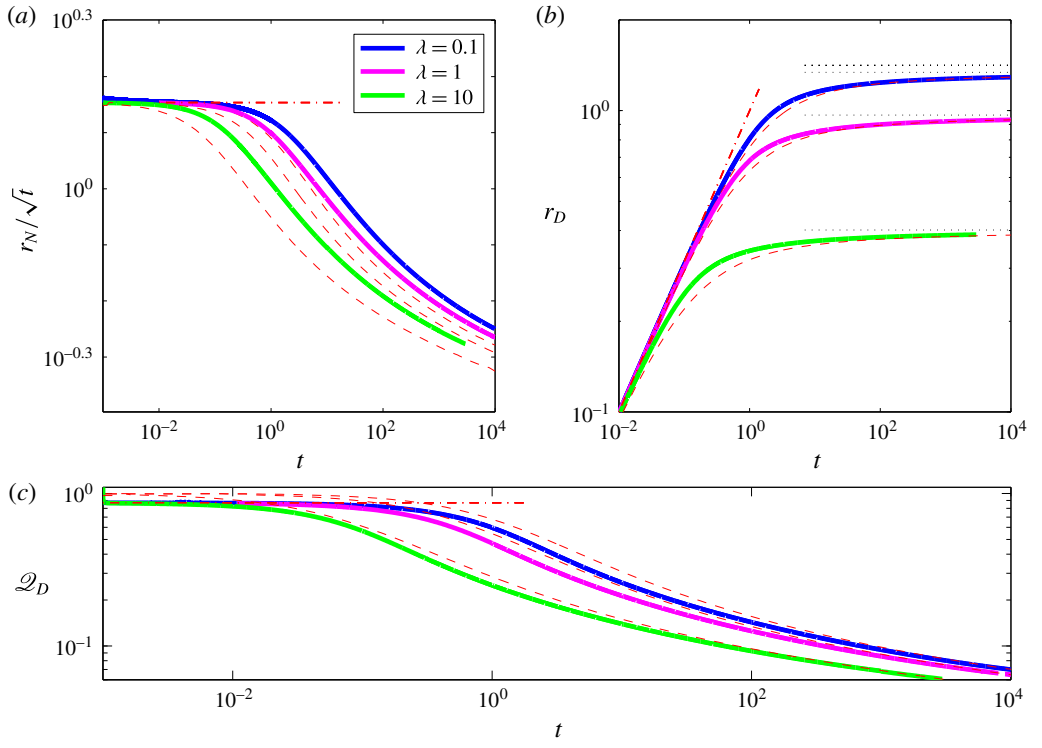

FIGURE 4. (Colour online) Evolution of the fluid front r_N (a), the drainage front r_D (b) and the horizontal flux at the drainage front $\mathscr{Q}_D$ (c) for $\mathscr{Q} = 1$ and for $\lambda = 0.1$, 1, 10, showing the full numerical solutions (thick curves), and the asymptotic estimate of the early time evolution (– –) and of the late-time evolution (– – – –).

where $y = y_D$ is defined by the relationship

$$h(r_D, t) = 1 = \xi_N^{2/3}(2\pi\mathscr{Q})^{1/4}\psi(y_D) \tag{2.15b}$$

and approaches to 1 asymptotically with $\mathscr{Q}$, implying that at early times the larger $\mathscr{Q}$ is, the closer r_D is to r_N. The corresponding flux at the drainage front

$$\mathscr{Q}_D \equiv -r_D \left.\frac{\partial h}{\partial r}\right|_{r_D} = -y_D \xi_N^{2/3}(2\pi\mathscr{Q})^{1/4} \left.\frac{\partial \psi}{\partial y}\right|_{y_D} \tag{2.15c}$$

is constant.

We use the solution (2.14) to initialize our numerical solutions and confirm that the predicted asymptotic structure is preserved at early times. In particular we find that the early time behaviour of the fluid and drainage fronts and of the flux at the drainage front follow the predictions in (2.14b), (2.15a), (2.15c) independently of the value of $\mathscr{Q}$ (figures 2b, 3) and independently of the value of λ (figure 4).

2.5. *Late-time evolution*

2.5.1. *The draining domain*

As the radius of the current expands, the extent of the drainage front increases and the drainage flux becomes comparable to the input flux. In this limit we may

anticipate an interior steady state in which leakage balances the input flux to leading order. We therefore look for steady solutions of (2.10*a*),

$$\frac{1}{r}\frac{\mathrm{d}}{\mathrm{d}r}\left(rh^3\frac{\mathrm{d}h}{\mathrm{d}r}\right)=\lambda h+1 \quad \text{for } r\leqslant r_D, \tag{2.16a}$$

subject to the imposed input flux at the origin, the height of the current equal to the critical drainage height at r_D and to a limiting flux $\mathscr{Q}_D$ to the outer current,

$$-rh^3\frac{\mathrm{d}h}{\mathrm{d}r}=\mathscr{Q} \quad \text{as } r\to 0, \tag{2.16b}$$

$$h=1 \quad \text{at } r=r_D, \tag{2.16c}$$

$$-r_D\frac{\mathrm{d}h}{\mathrm{d}r}=\mathscr{Q}_D \quad \text{at } r=r_D. \tag{2.16d}$$

In the limit $\lambda\ll 1$ we find the closed-form solution

$$h=[1+r^2-r_D^2-4\mathscr{Q}\ln(r/r_D)]^{1/4}, \tag{2.17a}$$

$$r_D=\sqrt{2(\mathscr{Q}-\mathscr{Q}_D)}, \tag{2.17b}$$

which has some similarity with the steady-state solution of a gravity current on a porous substrate with no critical entry pressure (Spannuth *et al.* 2009). The main difference in the solutions is the existence of a finite height of the current at the end of the drainage area, set by the capillary entry pressure in the present work, as opposed to the condition $h(r_D=r_N)=0$ in that previous work. This difference introduces a fundamentally different long-time behaviour, in which the fluid front in the present study propagates indefinitely.

The steady-state system (2.16) is second order in h and involves two unknowns (r_D and $\mathscr{Q}_D$), therefore four boundary conditions are required to solve it. The fourth relation can be provided by the solution to the outer current (§ 2.5.2), which leads to a full late-time solution (see § 2.5.3). Despite the missing information at this stage, reasonable progress can be made by assuming that at late time $\mathscr{Q}_D\ll\mathscr{Q}$, which results in the drainage front $r_D\approx\sqrt{2\mathscr{Q}}$ for non-dimensional critical thickness $\lambda\ll 1$. For general λ, equations (2.16*a*)–(2.16*d*) must be solved numerically (here with Matlab's bvp4c routine). For the numerical solution we substitute the boundary condition (2.16*b*) with the time derivative of the integral mass-balance relation (2.8)

$$2\pi\int_0^{r_D} v_p r\,\mathrm{d}r=\mathscr{Q}-\mathscr{Q}_D, \tag{2.18}$$

where $\mathscr{Q}_D=0$ and we use the analytic solution (2.17) in the limit $\lambda\to 0$ to verify the numerical solution. The results indicate that r_D increases with $\mathscr{Q}$ for any given λ, decreases with the increase of λ for any given $\mathscr{Q}$ and converges to the analytical solution (2.17*b*) in the limit $\lambda\ll 1$ (see figure 5). These steady-state solutions successfully predict the leading-order solution of the full equations under the assumption of zero flux at the drainage front (e.g. figure 2*a*).

2.5.2. *The non-draining domain*

The approach of the drainage front r_D to a steady position over time introduces an additional radial length scale, which at first suggests that the evolution of the non-draining part of the current can no longer be self similar. However, after sufficient time $r_D\ll r_N-r_D$ and to leading order the position of the drainage front can be

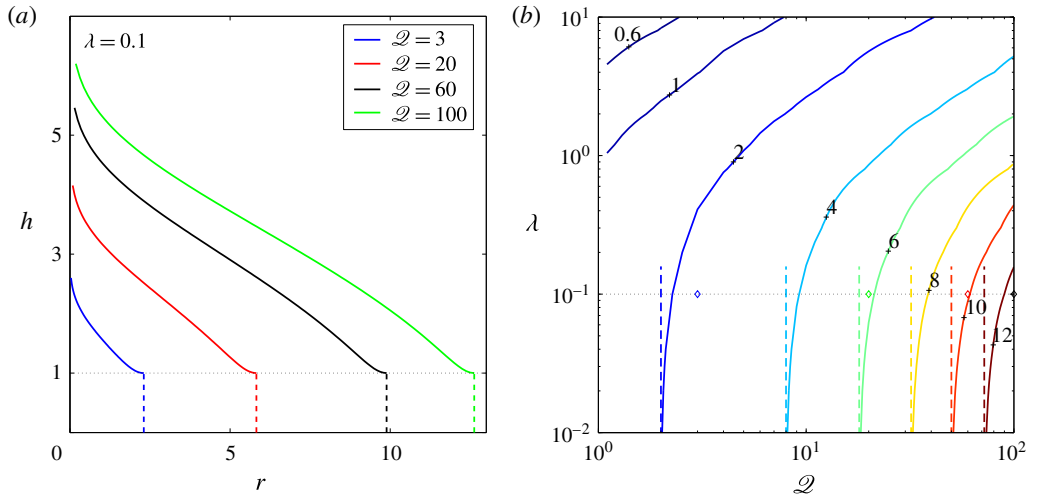

FIGURE 5. (Colour online) Numerical solutions to the steady-state boundary-value problem in the draining region (2.16). (*a*) Steady-state solutions of the free surface for $\lambda = 0.1$ and for $\mathscr{Q} = 3, 20, 60, 100$, where dash lines mark the position of the drainage front in each case. (*b*) Contours of the steady-state position of the drainage front r_D as a function of $\mathscr{Q}$ and λ (solid curves, contour value marked by adjacent numbers). In the limit $\lambda \ll 1$ the solution approaches $r_D = \sqrt{2\mathscr{Q}}$ (vertical dash lines). The $\diamond$ shapes along the $\lambda = 0.1$ grid line represent the points in the phase space that correspond to the solutions shown in (*a*). In all cases we assume that $\mathscr{Q}_D = 0$.

approximated as $r_D \approx 0$. In this limit, the radial length scale is effectively removed and we may anticipate that the flux $\mathscr{Q}_D$ past the drainage front is a slowly varying function of time, and that a similarity solution is indeed valid.

To investigate this asymptotic limit, we approximate the solution at the drainage front by matching the asymptotic solutions for the draining and non-draining currents at r_D. We first consider the propagation of the non-draining current for $r_D < r < r_N$, described by

$$\frac{\partial h}{\partial t} - \frac{1}{r}\frac{\partial}{\partial r}\left(rh^3\frac{\partial h}{\partial r}\right) = 0, \tag{2.19a}$$

with the boundary conditions

$$-rh^3\frac{\partial h}{\partial r} = \mathscr{Q}_D \quad \text{as } r \to r_D \approx 0, \tag{2.19b}$$

$$h = 1 \quad \text{as } r \to r_D \approx 0. \tag{2.19c}$$

The full numerical solution (§ 2.3) indicates that the approach to the steady state is slow, as the drop of the flux $\mathscr{Q}_D$ in time is approximately logarithmic, and that r_N grows nearly like $t^{1/2}$. This leads to the ansatz that the solution to (2.19) may be approximated by the similarity solution for a gravity current on an impermeable surface (2.14). Therefore, we let $\mathscr{Q}_D = \mathscr{Q}_D(s)$ and $h(r, t) = \zeta_N^{2/3}(2\pi\mathscr{Q}_D(s))^{1/4}f(x, s)$, where $s \equiv 1/\ln(t)$, $x = \zeta/\zeta_N$ and where $\zeta = r(2\pi\mathscr{Q}_D(s))^{-3/8}t^{-1/2}$ is a similarity

coordinate with $\zeta_N \equiv \zeta(r = r_N)$. Substituting these into (2.19) we find

$$\frac{x}{2}\frac{\partial f}{\partial x} + \frac{1}{x}\frac{\partial}{\partial x}\left(xf^3\frac{\partial f}{\partial x}\right) = \frac{s^2}{\mathscr{Q}_D}\left(\frac{3}{8}x\frac{\partial f}{\partial x} - \frac{f}{2\zeta_N^{2/3}}\frac{\partial \mathscr{Q}_D}{\partial s}\right), \tag{2.20a}$$

together with the boundary conditions

$$-2\pi\zeta_N^{8/3}xf^3\frac{\partial f}{\partial x} = 1 \quad \text{as } x \to 0, \tag{2.20b}$$

$$(2\pi\mathscr{Q}_D)^{1/4}\zeta_N^{2/3}f = 1 \quad \text{as } x \to 0. \tag{2.20c}$$

A scaling analysis of (2.20*a*) shows that the right-hand side is $O(s^2f/\mathscr{Q}_D,\ sf)$, while the left-hand side terms are $O(f)$ and $O(f^4/x^2)$. Therefore, as $t \to \infty$ ($s \to 0$) the dominant balance is independent of s and represented by the left-hand side of (2.20*a*), which has a similarity solution $f = \psi$ identical to (2.14) with a slowly time-dependent flux $\mathscr{Q}_D(s)$. Combining the similarity solution for r_N together with the boundary condition (2.20*c*) we find

$$1 = \zeta_N^{2/3}(2\pi\mathscr{Q}_D)^{1/4}\psi(x_D), \tag{2.21a}$$

$$x_D = \frac{r_D t^{-1/2}}{\zeta_N(2\pi\mathscr{Q}_D)^{3/8}}, \tag{2.21b}$$

where $x_D \equiv r_D/r_N$ and $\zeta_N = \xi_N$, which represents the relation between r_D and $\mathscr{Q}_D$ for the outer-spreading current.

Analytic approximated expressions may be found for (2.21) by noting that in the limit $x \to 0$, $f \sim (-\ln x)^{1/4}$. Hence, in this limit (for $x_D \to 0$) the inner limit of the outer-spreading current may be approximated as

$$h(r, t) = \left(-4\mathscr{Q}_D \ln\frac{rt^{-1/2}}{\zeta_N(2\pi\mathscr{Q}_D)^{3/8}}\right)^{1/4}, \tag{2.22}$$

which at the drainage front implies (using (2.19*c*)) that

$$1 = -4\mathscr{Q}_D \ln x_D. \tag{2.23}$$

2.5.3. *Asymptotic matching*

To determine the late-time behaviour of the current we estimate the position r_D and flux $\mathscr{Q}_D$ at the drainage front by matching the asymptotic solution at the draining domain, given by the numerical solution to (2.16) and (2.18), with that at the non-draining domain represented by (2.21) or by the approximation (2.23).

In the limit $\lambda \ll 1$ we obtain closed-form solutions by matching (2.17*b*) with the approximation (2.23),

$$1 = -2(2\mathscr{Q} - r_D^2)\ln\sqrt{\frac{r_D^2}{\zeta_N^2(2\pi\mathscr{Q} - \pi r_D^2)^{3/4}t}}, \tag{2.24a}$$

implying that $r_D \to \sqrt{2\mathscr{Q}}$ for $t \gg 1$, which is consistent with the steady-state solution with $\mathscr{Q}_D = 0$ (2.17*b*). When $r_D \ll \sqrt{2\mathscr{Q}}$ we predict that $r_D \approx \zeta_N(2\pi\mathscr{Q})^{3/8}t^{1/2}e^{-1/4\mathscr{Q}}$, which is consistent with the early-time behaviour (2.15*a*) up to a constant factor. Another analytical form with higher accuracy can be obtained using the approximation (2.21)

$$1 = \zeta_N^{2/3}(2\pi\mathscr{Q} - \pi r_D^2)^{1/4}\psi\left(\sqrt{\frac{r_D^2}{\zeta_N^2(2\pi\mathscr{Q} - \pi r_D^2)^{3/4}t}}\right), \tag{2.24b}$$

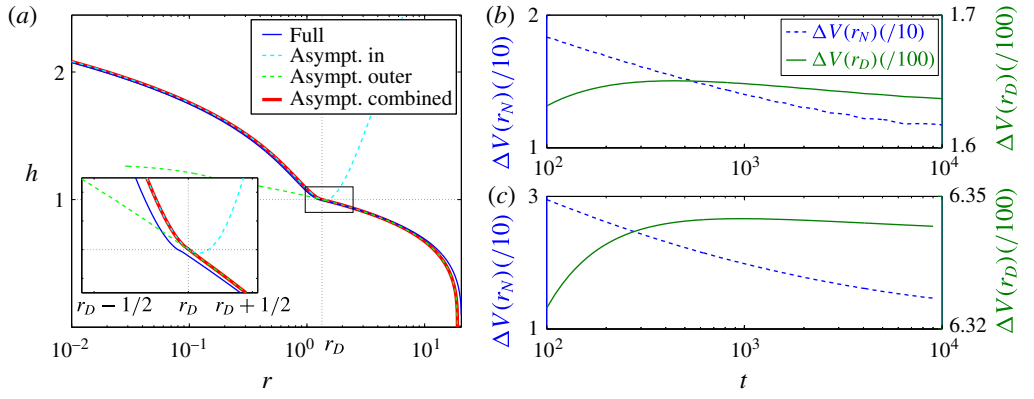

FIGURE 6. (Colour online) (*a*) Numerical solutions of the full equations for the thickness h for $\lambda = 0.1$, $\mathscr{Q} = 1$ at time $t = 10^3$ (—— blue) and the corresponding asymptotic solutions for $r < r_D$ (– – – – cyan), and for $r > r_D$ (– – – – green). The solution that results from matching at r_D is marked by (—— red). Insets zoom into the vicinity of the drainage front. (*b*,*c*) The evolution of the volume difference normalised by the total volume, between the numerical and asymptotic solutions of the percolating region $r \leqslant r_D$ (—— olivegreen) and of the whole current $r \leqslant r_N$ (– – – – blue), for $\mathscr{Q} = 1$ (*b*) and $\mathscr{Q} = 10$ (*c*).

which is also consistent with $r_D \to \sqrt{2\mathscr{Q}}$ for $t \gg 1$ (figure 3*a*). This late-time asymptotic solution predicts the early-time behaviour of the two fronts to high accuracy, and it also predicts quite accurately the early-time evolution of $\mathscr{Q}_D$ in limit $\mathscr{Q} \ll 1$.

For general λ the asymptotic closed-form relation (2.17*b*) is no longer valid. In this case, we obtain an asymptotic relation for the inner part by solving the system (2.16) for a specified range of $\mathscr{Q}_D$ and a given λ, which leads to a numerical mapping between r_D and $\mathscr{Q}_D$ that generalizes (2.17*b*) for any λ. Matching this asymptotic prediction for the inner region with that of the outer region provides a better agreement with the full numerical solution for small but finite λ (figures 2*b*, 3, black dash line), and shows very good agreement with the early and late-time evolution of the full numerical solution for larger values of λ (figure 4). It should be noted that as the flux to the exterior current $\mathscr{Q}_D$ reaches it's asymptotic form, there is an additional time needed for the fluid front r_N to attain the corresponding position. This results in the excellent agreement by $t = 10^4$ in figures 3(*b*) and 4(*c*), and the much slower approach to the asymptotic solution for r_N in figures 2(*b*) and 4(*a*).

Together with the corresponding solution for $\mathscr{Q}_D(t)$ and r_D, we determine the thickness h and the front r_N following the similarity solution for a gravity current on impermeable surface, which results in the quasi-self-similar solution

$$h(z, t) = \zeta_N^{2/3}[2\pi\mathscr{Q}_D(t)]^{1/4}\psi(z), \tag{2.25a}$$

$$r_N = \zeta_N[2\pi\mathscr{Q}_D(t)]^{3/8}t^{1/2}, \tag{2.25b}$$

in which there is an implicit time dependence in $\mathscr{Q}_D$ that is absent in the classical solution for a gravity current on impermeable substrate. Overall, we find that the asymptotic predictions of r_N, r_D, $\mathscr{Q}_D$ and h are in good agreement with the full numerical solution (figures 2–4 and 6). We estimate the convergence to the asymptotic

solution by computing the evolution of the normalised volume difference of the numeric and asymptotic solutions

$$\Delta V(r_i) = \frac{\displaystyle\int_0^{r_i(t)} r|h(t)_{numeric} - h(t)_{asymptotic}|\,\mathrm{d}r}{\displaystyle\int_0^{r_i(t)} rh(t)_{numeric}\,\mathrm{d}r}, \tag{2.26}$$

where $r_i = r_D$ or r_N (figure 6*b*,*c*). This indicates that by $t = 10^4$ the convergence of the interior current ($r \leqslant r_D$) can be 10 times better than that of the exterior current, which again demonstrates the time needed for the exterior flow to adjust to changes that occur near the draining front.

3. Experimental validation

To test the theoretical results we have conducted a series of laboratory experiments in which a viscous fluid was injected onto a thin, perforated metal plate. The resultant viscous gravity currents propagated along, and drained through, the thin porous plate allowing direct comparison with our theoretical model. The viscous fluid used was Lyle's golden syrup mixed with water to modify the viscosity and with titanium dioxide (0.2 % in weight) to make the fluid optically opaque for imaging. Perforated sheets of steel were used as the porous substrate, with a thickness of $b = 0.75$ mm and pore diameter $d_p = 1$ or 2 mm. To fully characterize the system we first conducted a suite of drainage experiments, described in § 3.1, in which we measured the effective permeability of the porous plate. This enables us to make quantitative predictions of the propagation and drainage from viscous gravity currents in § 3.2. Experiments took no more than a few minutes each and there were no significant heat sources near the apparatus. Therefore, within an experiment we assume that temperature variations were negligible and that quantities such as viscosity and surface tension were uniform and remained constant.

3.1. *Measuring the permeability of the substrate*

The permeability of a porous plate templated by a regular lattice of cylindrical holes should, in principle, be amenable to robust theoretical estimates. However, since the mesh is thin compared with the pore diameter, any putative Poiseuille flow through the pores may not be fully developed and the detachment or dripping of fluid from the base may similarly affect the flux. Hence, an empirical characterization of the permeability is required.

The experimental apparatus consisted of a cylindrical tank of diameter $d = 9.3$ cm that had an open end at the top and a bottom end that was covered with a disk of the perforated sheet of thickness b (figure 7*a*). We mounted the cylinder vertically and filled it with the viscous fluid to height $h_0 > h_D$, while its bottom end was covered with a removable seal. At $t = 0$ we removed the seal abruptly, allowing the fluid to drain through the mesh into a beaker placed on the scales that monitored its weight m. The instantaneous mass of the fluid in the cylinder is therefore $M(t) = M_0 - m(t)$, where $M_0 = \pi d^2 \rho h_0/4$ is the initial mass, so that the evolution of the height in the cylinder is $h(t) = h_0(1 - m(t)/M_0)$ by mass conservation. By the time the fluid level reached the bottom of the cylinder, a thin film remained attached to the walls of the cylinder with mass initially equal to approximately 15 % of M_0. We accounted for that

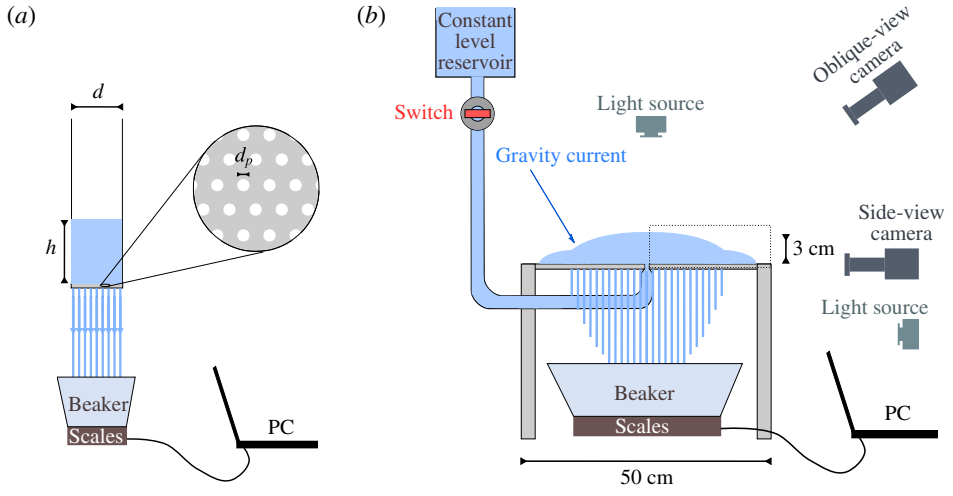

FIGURE 7. (Colour online) Diagrams of the experimental apparatus. (*a*) Apparatus to measure the permeability of the substrate is composed of a cylindrical tube of diameter d with an open end at the top and a bottom end made of a steel mesh of thickness b and holes of diameter d_p. Viscous fluid that was contained in the cylinder drained across the mesh into a beaker whose mass was monitored. (*b*) In an apparatus for a gravity current over a porous substrate the same fluid is discharged at constant flux over an identical mesh. The evolution of the current was imaged from oblique and side views via synchronized cameras, and the drainage flux was monitored throughout the experiment. To acquire a side view of the drainage pattern, an additional light source was required. A zoom into the cross-section of the gravity current inside the dotted rectangular is schematically shown in figure 1.

loss by using $\overline{M_0} \equiv m(t_{final})$ instead of M_0 in the computation of the evolution of the hydrostatic head that drives the flow,

$$h(t) = h_0 \left(1 - \frac{m(t)}{\overline{M_0}}\right). \tag{3.1}$$

The experimental measurements, plotted as $h(t)$ in figure 8 imply a nearly exponential behaviour. The evolution of the height of the fluid column in the cylinder can be predicted using conservation of mass,

$$\frac{\partial h}{\partial t} = -v_p = -\phi \frac{kg}{b\nu}(h + b), \tag{3.2}$$

which has an exponential solution

$$h(t) = (h_0 + b)e^{-\tau t} - b, \tag{3.3}$$

where $\tau = \phi kg/b\nu$ is the characteristic drainage time. Using a viscometer we found the kinematic viscosity to be $\nu = 31.66 \pm 0.06$ cm^2 s^{-1}. We then obtained the effective permeability ϕk by computing a regression to the experimental data (figure 8), which resulted in an expected difference from the simple Darcy drainage model. The pore Reynolds number in this case is estimated as

$$Re = \frac{v d_p}{\nu} \simeq 10^{-3}, \tag{3.4}$$

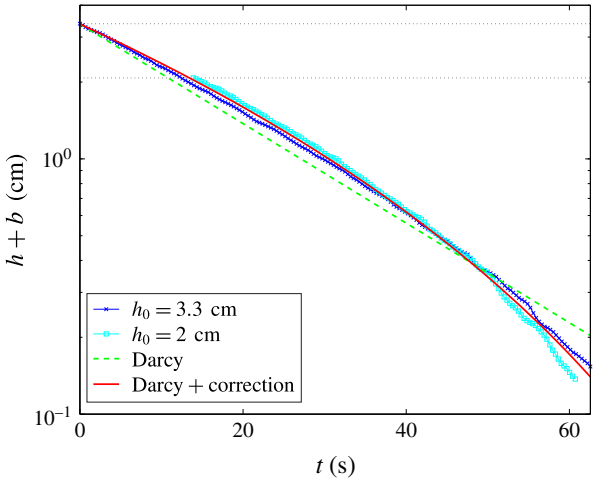

FIGURE 8. (Colour online) Evaluation of the permeability k from one-dimensional percolation experiments using the apparatus shown in figure 7(*a*). Experiments were initiated with heads $h_0 = 3.3$, 2 cm ($\times$ and $\square$, respectively). Uncertainties of the thickness measurements are of the order of 10^{-2} cm. Regression is computed initially using Darcy's law (– – – –), and then using an effective percolation law (3.5), which is Darcy to leading order (——).

where we take $v = 0.2$ cm s^{-1} and $d_p = 0.1$ cm, implying that the flow should be well within Darcy's regime. The discrepancy from Darcy's law is therefore introduced through additional, weaker processes beside percolation. A potential cause is the interaction of the viscous fluid that emerges out of the base of the substrate with an air interface that is present under the substrate. Owing to strong capillary interactions along that interface the detachment of fluid from the substrate becomes complex, involving drops and jets in a spatio-temporally varying pattern, which appears to be stochastic (Pirat *et al.* 2004).

Given that the leakage follows Darcy's law to leading order, we account for the complex drainage pattern by specifying an effective percolation law of the form

$$\overline{v_p} \equiv -\tau (h+b)^{1-n}, \tag{3.5}$$

where the parameter n, to be found by regression, is expected to be smaller than 1 since the percolation is expected to follow Darcy flow to leading order. The solution to (3.2) with the effective percolation (3.5) is

$$h = [n(h_0+b) - n\tau t]^{1/n} - b, \tag{3.6}$$

and regression to the experimental data with n as an additional free parameter results in $\phi k \approx 10^{-4} \pm 5 \times 10^{-7} \times \text{cm}^2$ and $n \approx 0.26 \pm 0.014$ (uncertainties represent the 95 % confidence interval), which is consistent with our expectation of $n < 1$ (see figure 8). The percolation law may therefore be approximated as

$$\overline{v_p} = -\tau (h+b)[1 - n \log(h+b)] + O(n^2), \tag{3.7}$$

which reflects a Darcy behaviour to leading order and a correction proportional to n that is likely introduced by the complex leakage pattern at the bottom of the porous plate. The first-order correction to the percolation law is included in the full numerical simulation that predicts the experiments performed in the following section.

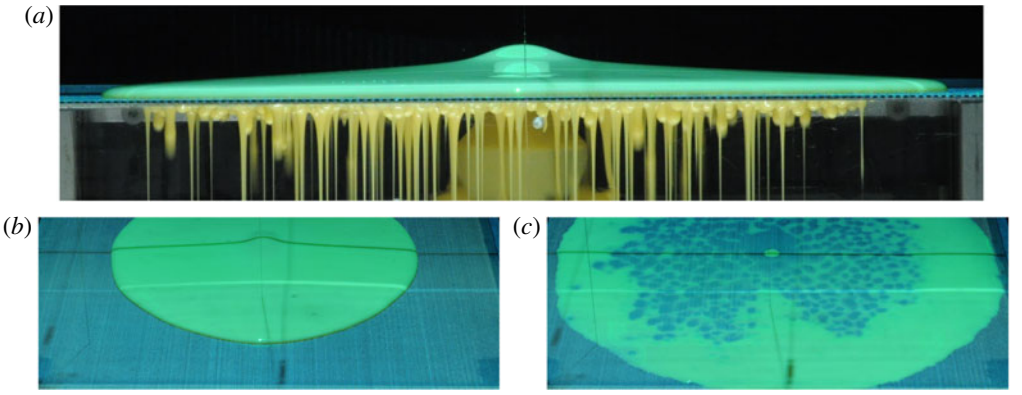

FIGURE 9. (Colour online) Snapshots from experiment A (table 1) of a viscous gravity current over a porous substrate with finite entry pressure. (*a*) Side view of the current showing the surface current and the draining fluid underneath the substrate and the gap between the positions of the drainage and the fluid fronts. (*b*) An oblique view of the surface current at the time corresponding to that of the image in (*a*). (*c*) An oblique view of the substrate at the end of the experiment ($Q = 0$), showing the inner region where drainage was active and the outer ring of fluid that has not broken through the critical entry pressure.

3.2. *Gravity current experiments*

We conducted a suite of experiments of viscous gravity currents propagating over a thin porous mesh, the results of which are summarized in table 1. The experimental apparatus consisted of a fluid reservoir, which provided a constant hydraulic head and hence constant flow rate, and a horizontal, perforated sheet of steel (50×50 cm^2), identical to the one used in § 3.1, on which the injected fluid could propagate (figure 7*b*). Experiments were initiated by turning a valve on, which discharged fluid from the reservoir through a circular nozzle 15 mm in diameter and located in the centre and at the same level of the perforated sheet. The relatively small thickness of the perforated sheet that we used ($b = 0.75$ mm) compared with its length (500 mm across), resulted in some deformation of the substrate due to the weight applied by the propagating current. Deformation of the substrate often lead to local variations in the thickness of the current, and hence to variations in the local leakage flux through the porous plate, both of which resulted in some currents propagating in a non-axisymmetric mode (see figure 13 for example). To keep the thin perforated sheet flat, we suspended the thin substrate from below and above at several locations with fishing line. This provided a support to the substrate, in addition to the support at the centre of the sheet by the nozzle and along its rim by a transparent frame.

With this experimental arrangement, the viscous fluid propagated axisymmetrically over the perforated sheet, and leaked through the sheet, where the capillary entry pressure was exceeded. The drained fluid was collected in a beaker whose weight was continuously monitored. The evolution of the current was imaged by a side view camera that was aligned with the plane of the substrate so that it captured both the surface current and the draining fluid (see figure 9*a*). Another camera took images from an oblique angle above the substrate (figure 9*b*,*c*). Both cameras operated at a rate of 2 frames per second and were triggered simultaneously.

Experiment	Q ($cm^3\ s^{-1}$)	ν ($cm^2\ s^{-1}$)	ρ ($g\ cm^{-3}$)	h_D (mm)	T (°C)	λ	$\mathscr{Q}$	$\mathscr{T}$ (s)
A	24.6	25.5	1.403	4	—	5.3	10.7	5.2
B	43.6	24.7	1.4	4.7	20	6.3	13.3	3.4
C	36.6	29	1.4	4.7	18.5	6.3	14.4	5.3
D	22.5	42.4	1.41	4.77	20.2	6.35	22	5.5

TABLE 1. Parameters of the gravity current experiments.

In preliminary experiments, we tested two types of perforated sheets having pore diameters $d_p = 1$ and 2 mm. This property appeared to have a large effect on the entry pressure (2.6) and on the percolation through the substrate (3.4). In experiments using the larger pore-diameter sheet, we could not access conditions in which there was a measurable difference between the drainage and the fluid fronts, suggesting a small or negligible capillary entry pressure. In contrast, using the smaller pore-diameter sheet leakage had hardly initiated by the time the fluid front had reached the edge of the apparatus, suggesting that the capillary entry pressure was too large for leakage to occur. Therefore, in order to observe and measure the intermediate regime, in which $0 < r_D < r_N$, we used the sheet with the smaller pore diameter and partially prewet it with a small volume of water (smaller than the total pore volume) which was sprayed uniformly on the substrate before the initiation of an experiment. We emphasise that the surface tension coefficient of the fluid used for partial prewetting is smaller by 10 % with respect to the current fluid. We found that the partial prewetting of the porous sheet had the effect of producing an intermediate critical depth.

We performed several experiments as shown in table 1. For each experiment we obtained a series of side-view snapshots (e.g. figure 9*a*), from which we measured the evolution of the drainage and of the fluid fronts (figure 10). The side-view images (see supplementary movie 1 available at http://dx.doi.org/10.1017/jfm.2016.412) reveal a complex leakage pattern through the substrate, showing drops and jets that alter spatio-temporally throughout the experiment. The oblique-view camera (see also supplementary movie 2) was used to confirm the axisymmetry of the flow throughout the experiment (e.g. figure 9*b*), but it also revealed other aspects of the complex leakage pattern (figure 9*c*), which we discuss in the next section. The measurement error of r_N, defined as half the width of the region over which the fluid colour transits to the background colour, is approximately 1 mm. Measurement error of r_D, defined as half the width of a fluid jet or drop, is approximately 3 mm. The temporal uncertainty of each measurement, estimated as half the interval between two successive images, is approximately 0.25 s.

In most of the experiments the current could not evolve to the late-time phase in which the drainage front reached a steady position since the extent of r_D was comparable to the size of the apparatus. However, in experiment A (figure 10*a*) we were able to measure a significant deceleration of the drainage front, which indicates an approach to a steady position. These experiments also indicated that the early-time evolution of the fluid front followed the expected $t^{1/2}$ power law, while the detailed dynamics of fluid invasion into the pores and detachment of drips from the underside of the porous plate (neither of which we attempt to capture in the simple theory) resulted in a drainage front which did not exhibit power-law behaviour (figure 11). More precisely, the drainage front seemed to lag behind the theoretical value at early time, despite having a larger acceleration.

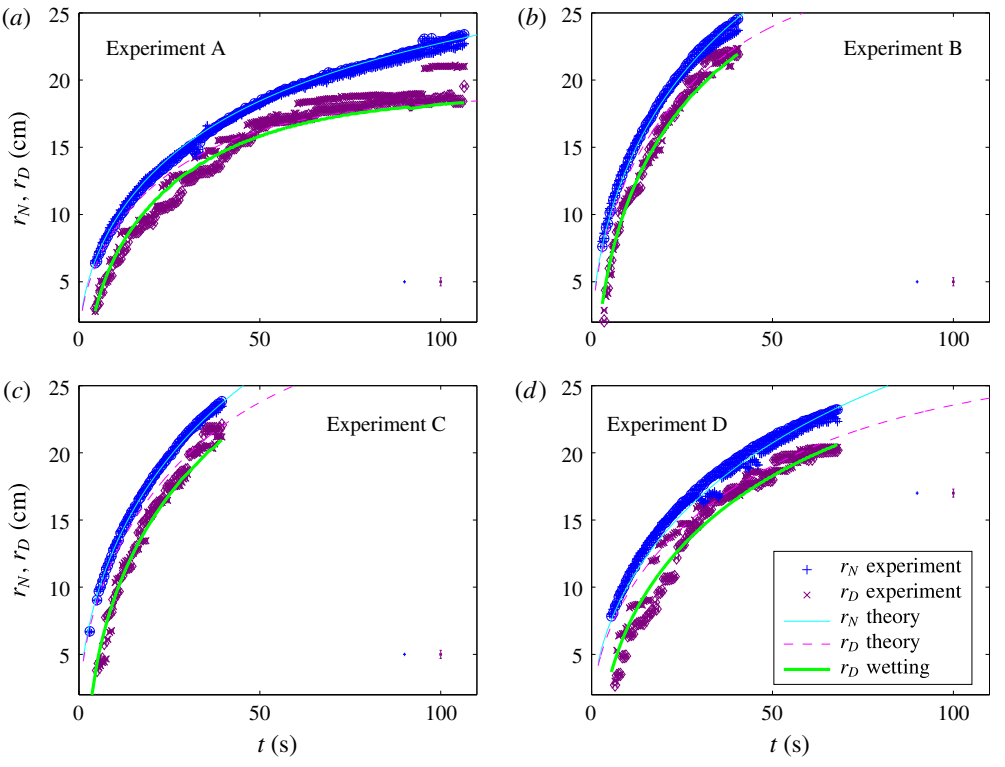

FIGURE 10. (Colour online) Experimental measurements and theoretical predictions of r_N ($\bigcirc$, $+$) and r_D ($\diamond$, $\times$) for gravity currents with parameters given in table 1, where the two symbols denote the left and the right fronts (see figure 9*a*) respectively. Error bars for r_N and r_D are shown on the bottom right corner in corresponding colour. The theoretical predictions are marked with —— (cyan) and – – – – (magenta) for the fluid and drainage fronts. A correction to the early-time evolution of the drainage owing to finite-time wetting of the substrate is marked with —— (green).

To quantitatively compare the experimental results with the theoretical predictions, we computed the numerical solution for the dimensionless parameter $\mathscr{Q}$ and λ specified in table 1, accounting for the non-Darcy correction to the percolation law (3.7). Estimating the dimensionless quantities requires determination of the value of the critical entry thickness h_D, and particularly the quantity $4\gamma\cos\theta$ in (2.6). Since the fluid is over 99 % Lyle's golden syrup, the surface tension coefficient is approximately $\gamma \approx 80$ dyn cm^{-1} (Llewellin, Mader & Wilson 2002), which is similar to the surface tension coefficient of water (72 dyn cm^{-1}). We therefore make the assumption that the contact angle of golden syrup on steel is similar to that of water on steel. The latter can vary significantly depending on the substrate surface energy and texture (e.g. 55–97° (Boulange-Petermann, Gabet & Baroux 2006); conversion from advancing and receding to Young contact angles following Tadmor (2004)), implying that h_D may be in the range of 1–13 mm, which is consistent with our observation (see for example, figure 12*b*). Within that range we use the contact angle as a tuning parameter to fit the theoretical predictions.

The source flux Q was measured by two methods. The first was based on measuring the drained mass of fluid, in a manner similar to the method described in § 3.1.

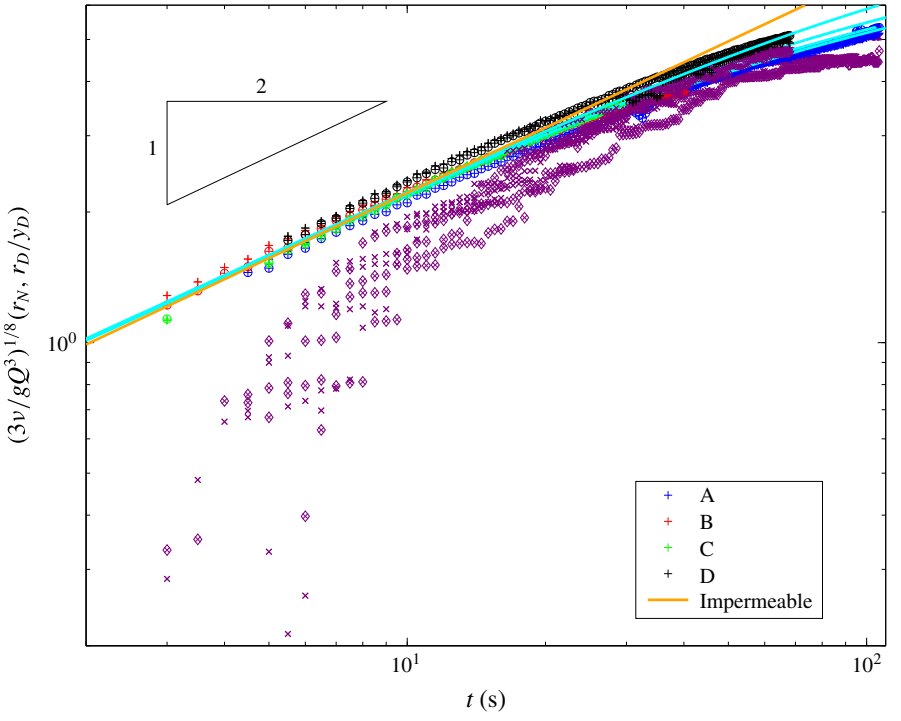

FIGURE 11. (Colour online) Measurements of the fronts r_N (+, ∘, blue, red, green and black) and r_D (◇, ×), where the two symbols denote the left and the right fronts, of gravity currents with parameters given in table 1, normalized with respect to the early time solutions (2.14*b*) and (2.15*a*) respectively. The solution for a constant-flux gravity current on an impermeable surface (—— orange) is shown for reference, and the theoretical predictions for the fluid front r_N are shown (—— cyan).

However, this measures $Q - Q_D$ and in most experiments the drainage front did not reach its asymptotic value $r_D(t \to \infty)$ and therefore a credible measurement of Q could not be achieved with this method. A method that produced a more reliable measurement was based on the known solution for a gravity current on impermeable substrate (Huppert 1982). Specifically, as long as the flux through the substrate is small compared with Q, which is the case in early time, the fluid front should follow to leading order the early-time solution (2.14*b*), which in dimensional form is

$$r_N = \xi_N \left(\frac{gQ^3}{3\nu}\right)^{1/8} t^{1/2}. \tag{3.8}$$

Scaling r_N by the coefficient of the right-hand side of (3.8), should therefore result in the collapse of the measurements of all the experiments to a single curve $\xi_N t^{1/2}$. Using the quantities we measured (table 1) we find that indeed measurements of r_N of all the experiments scale at $t^{1/2}$ during the early-time evolution and that by fitting Q they collapse to the same curve (figure 11). This early-time collapse therefore supports our analysis that leakage is initially a secondary effect, and provides a robust estimate of the input flux which can be subsequently used to test our model predictions against the experimental data in the region where leakage plays a leading-order role. The

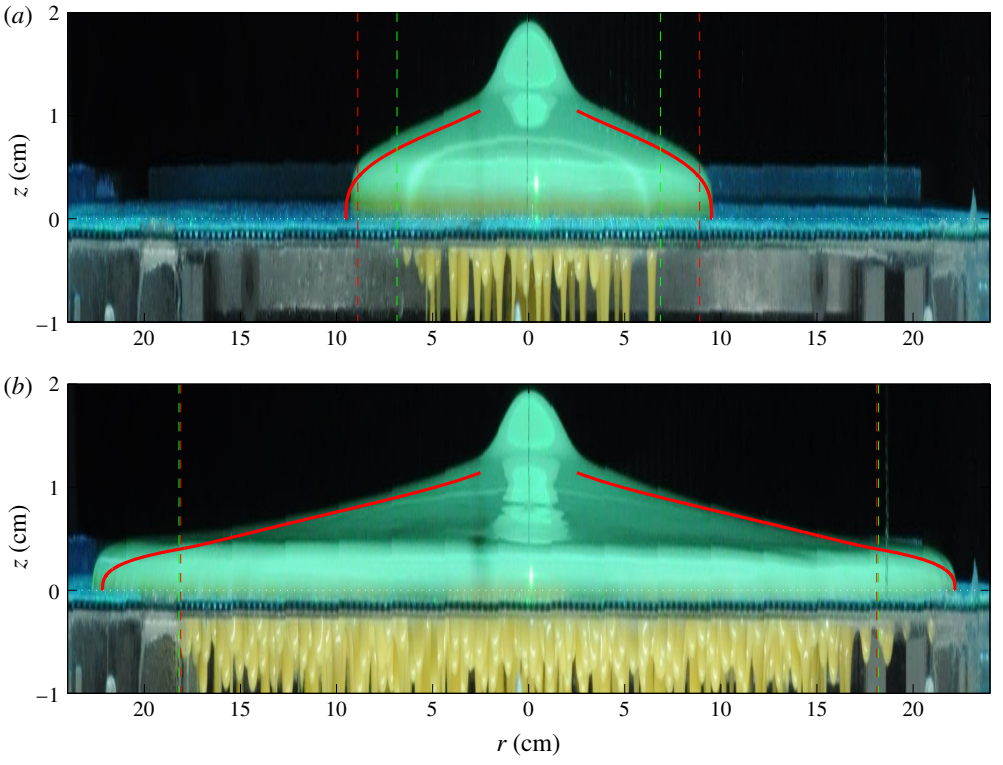

FIGURE 12. (Colour online) Snapshots from side view from experiment A (table 1) at $t = 10$ s (a) and at $t = 100$ s (b). The theoretical prediction of h is shown (——) and the corresponding predictions of the drainage fronts are shown in – – – – (red) for the wetting-excluded theory and in – – – – (green) for the delayed-wetting correction. The position $z = 0$ is the top surface of the substrate at the centre (– – – – yellow).

fitted values for Q differ from the measurements of the flux via the drained-fluid method by 9 % in the case of experiment A, in which the drainage front decelerated substantially compared with the other experiments. In contrast, the drainage front in the other experiments was far from its steady-state limit and so the difference in the measurement of Q between the two methods was larger (28 % for experiments B and D and 40 % for experiment C).

Obtaining the flux for each experiment using (3.8), we then use the critical capillary entry pressure to fit both the drainage and the current fronts along the entire temporal interval. The results of the comparison show good agreement between theory and measurements for the fluid front and for the late-time evolution of the drainage front (figure 10). A corresponding comparison of the current thickness also demonstrates consistency between the theory and the experiments (figure 12).

As indicated earlier, a discrepancy exists between the theory and the measured evolution of the drainage front r_D at early times. The difference between the predicted and measured values is larger than the error in the measured position (figure 10), which implies that additional physical processes need to be accounted for in the initial drainage. Before an experiment initiates, the pores of the substrate contain air. Once the critical depth is reached and leakage initiates, the fluid wets the pores of thickness b, and pushes the air away. After that wetting phase, when the pores are

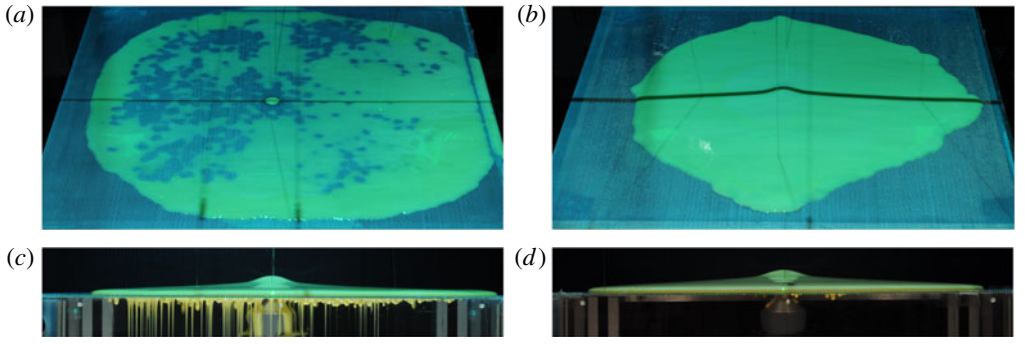

FIGURE 13. (Colour online) Snapshots from several experiments that we did not include in the analysis. In these experiments drainage was either non-uniform or did not initiate, possibly because the porous substrate was not sufficiently levelled or because the entry pressure was too high. (*a*) Snapshot after the termination of an experiment in which percolation did not initiate on the right half. (*b*) Strongly non-axisymmetric surface front, (*c*) Side view of the experiment in (*a*) at an earlier time, showing weaker drainage on the right side. (*d*) Side view of an experiment where percolation did not initiate throughout the flow.

saturated with the viscous fluid, the percolation is governed by the effective Darcy's law (3.7). The simplified theory in § 2.1 accounts for the percolation of a saturated porous substrate but does not include a description of this initial wetting process. We therefore include a delay term in the propagation of the drainage front in the original, wetting-excluded theory, accounting for fluid filling the pore space. We assume that the delay term is proportional to the velocity of the drainage front and has a characteristic time scale denoted by $\mathscr{T}$. Specifically, the difference between the predicted and measured positions of the drainage front is

$$r_D^{predicted} - r_D^{measured} = \dot{r}_D \mathscr{T}. \tag{3.9}$$

Fitting (3.9) to the experimental measurements of the drainage front with $\mathscr{T}$ as a free parameter results in a much better agreement with the experiments (figure 10), where the characteristic delay time is $\mathscr{T} = 4.85 \pm 0.97$ s (table 1). This time interval is comparable to the percolation time scale $bv/\phi kg \approx 20$ s.

4. Discussion

The theoretical, numerical and experimental investigation of the previous sections have demonstrated that finite capillary entry pressure can have a leading-order effect on the drainage of viscous fluids into porous substrates. Previous studies, in which there was no capillary entry pressure, have shown that a finite extent is reached for either two-dimensional or axisymmetric spreading (e.g. Pritchard *et al.* 2001; Spannuth *et al.* 2009). This steady state is reached when the input flux is balanced by the leakage flux, and is characterized by having a zero fluid depth at the drainage front of the current. In stark contrast, for the currents considered here, the finite capillary entry pressure imposes a finite current depth at the edge of the drainage region. As a consequence, there is always a residual flux of fluid beyond the region of leakage, and hence a viscous current propagating into the far field. The implication

being that, despite a leading order balance between the input flux and leakage, fluid continues to propagate far from the injection point.

Evaluation of the experiments in § 3.2 using the viscous theory presented in § 2 demonstrates the influence of the capillary entry pressure in restricting leakage to a finite region beyond which an undraining current continues to propagate. However, this evaluation requires a validation that the underlying assumptions of the theory are satisfied during the experiment. Particularly, $Re \ll 1$ has to be satisfied throughout the flow. We evaluate Re at the nozzle, assuming that it represents an upper limit to Re throughout the flow. The nozzle has a cone shape that fits the feeding pipe of radius $\bar{R}$ at one edge, and has a narrower edge of radius R, from which the fluid is discharged at velocity U onto the perforated sheet. The flux Q from the feeding pipe and into the nozzle can be estimated via Poiseuille's law $Q = \pi \bar{R}^4 \Delta p / 8\nu\rho L$, where L is the length of the feeding pipe, $\Delta p = \rho g \bar{b}$ is the pressure drop and $\bar{b}$ is the head. Conservation of mass implies that $U = Q/\pi R^2$, therefore Re at the nozzle outlet is

$$Re = \frac{UR}{\nu} = \frac{g\bar{b}\bar{R}^4}{8L\nu^2 R}. \tag{4.1}$$

Using $\bar{b} = 22$ cm, $\bar{R} = 1.27$ cm, $R = 0.75$ cm, $L = 120$ cm, and $\nu = 20$ cm^2 s^{-1} the lowest kinematic viscosity, we find that $Re \approx 0.2$. Moreover, a valve that was positioned between the head and the feeding pipe was only partially open, so the flux in our experiments was lower than the maximum that the system could provide. Therefore the actual upper limit on Re was even lower than that estimated above, which confirms that our experiments were well within a viscous-dominated regime.

A major component of the discrepancy between our theory and experiments is the initial flow through the porous substrate. The finite thickness of the substrate resulted in additional capillary interactions between the viscous fluid and the underlying layer of air. This led to an apparent stochastic pattern of leakage, involving complex interactions of drops and jets that vary spatio-temporally along the bottom side of the metallic mesh. A reflection of that complex leakage is also seen in the oblique angle images that were taken after the termination of experiments, which revealed a non-axisymmetric drainage front and a leakage region composed of a distributed spot pattern (figure 9*c*). These spots, having a typical diameter of $\sim$10 pore diameters, were regions where fluid was either completely drained or was suspended on the substrate in a very thin and transparent layer of fluid. This pattern of leakage may contribute to the non-Darcy percolation that we measured, and although it seem to introduce a relatively small correction to Darcy's law, such interactions may become important in other set-ups (Pirat *et al.* 2004).

Additional discrepancy in the early time evolution of the drainage front was attributed to the finite wetting time of the partially prewetted pores. This resulted in a time delay, which implied a significant correction to the prediction of the drainage front position. However, we expect this delay to be less important to the propagation of the fluid front because the delay is mostly significant in early time, in which most of the fluid flux contributes to the surface current. We note that the solubility of syrup and water could modify the viscosity of the draining fluid and impact the flow time scales. This may be a source of discrepancy if the solubility time scale, which is difficult to quantitatively constrain, is short compared with the time scale of wetting of the partially water-prewetted pores by the syrup that is approximately given by the delay time scale $\mathscr{T} \approx 5$ s. We should also emphasize that the wetting-induced delay was not an issue in the measurement of permeability (§ 3.1) because in that case the

substrate pores became saturated by the time the experiment was initiated. Future studies should account for the wetting phase in more detail, taking into account the spreading of the fluid in the cylindrical pores (e.g. Davis & Hocking 2000).

5. Conclusions

The propagation of a viscous gravity current over a porous substrate with finite entry pressure results in two distinguished flow regimes; an inner domain in which drainage through the substrate is active and an outer domain in which there is no drainage. Consequently, the flow involved two time-dependent fronts, one at the interface between the two regions and another at the nose of the current. An asymptotic analysis near the drainage front turns out to be powerful in predicting the evolution of the entire current at early, intermediate and late times. Specifically, we find that the draining portion of the current approaches a steady-state solution logarithmically in time, which can be approximated quite accurately by solving a steady-state boundary value problem. In addition, the non-draining part has a quasi-self-similar solution, which has an identical structure to the self-similar solution of gravity current on impermeable surface (Huppert 1982), but with a time-dependent input flux. This implies that in the flow we consider, the front of the surface flow would, in principle, never stop. The experiments revealed additional physical processes that may be important in a number of practical applications, including stochastic leakage pattern at the exit of the porous substrate and a significant leakage delay despite the relatively thin substrate that was used. Accounting for these processes we find that our theory is consistent with the experimental measurements.

The main result of this work is that when capillary forces inhibit fluid invasion into a porous substrate, fluid may propagate indefinitely even when the leakage flux and input flux balance to leading order. This result has implications for the region over which a spill may accumulate in industrial settings, and the distance over which environmental or geophysical flows may propagate.

Acknowledgements

We thank M. Hallworth, C. Hitch and D. Page-Croft for assisting with technical aspects of the experiment; Y. Ashkenazi for computational resources on Tsia; discussions with H. Huppert, J. Lister, S. S. Pegler, L. Prigozhin, I. Rubenstein, M. G. Worster, B. Zaltzman. R.S. thanks SIDEER and BIDR in Ben-Gurion University, Israel, for financial support, and to DAMTP, University of Cambridge, UK, where some of this research took place. J.A.N. acknowledges support from a Royal Society University Research Fellowship.

Supplementary movies

Supplementary movies are available at http://dx.doi.org/10.1017/jfm.2016.412.

Appendix A. The numerical solver

Solving equations (2.10) on a single domain $r \in [0, r_N]$ is computationally expensive if we wish to investigate the long-time asymptotic behaviour, as the moving front requires a growing number of nodes with time. Instead, we split the domain into two sub domains at the interface $r = r_D$, map each of the subdomains into the interval [0, 1], in which the free boundaries become stationary positions, and solve (2.10) in

the two subdomains simultaneously. Applying the mapping $r \to r/r_D$ in the percolating (inner) region ($0 \leqslant r \leqslant r_D(t)$), and $r \to (r - r_D)/(r_N - r_D)$ in the impermeable (outer) region ($r_D(t) < r \leqslant r_N(t)$) leads to a partial differential equation for the evolution of the free surface in both domains

$$\frac{\partial h}{\partial t} - \frac{\partial h}{\partial r}\frac{r\dot{A} + \dot{B}}{r_I(1-C)} - \frac{1}{r_I^2[r(1-C)+C](1-C)^2}\frac{\partial}{\partial r} \times \left[(r(1-C)+C)h^3\frac{\partial h}{\partial r}\right] = -P(\lambda h + 1), \tag{A 1}$$

where $r \in [0, 1]$. For the permeable regime we set

$$r_I = r_D, \quad \dot{A} = \dot{r}_D, \quad \dot{B} = 0, \quad C = 0, \quad P = 1, \tag{A 2a–e}$$

and for the impermeable regime we set

$$r_I = r_N, \quad \dot{A} = \dot{r}_N - \dot{r}_D, \quad \dot{B} = \dot{r}_D, \quad C = \frac{r_D}{r_N}, \quad P = 0. \tag{A 3a–e}$$

The mapping into two fixed intervals requires two evolution equations, one for each front. The outer front evolves kinematically,

$$\dot{r}_N = \frac{q}{h} = -\frac{1}{3(r_N - r_D)}\left.\frac{\partial h^3}{\partial r}\right|_{r=1}, \tag{A 4a}$$

in terms of the mapped coordinates, where the spatial derivative is evaluated using the two nearest nodes and the boundary condition $h(r_N) = 0$, thus providing second-order accuracy. For the inner front we obtain an evolution equation by taking the time derivative of the boundary condition (2.10*c*) and then substituting $\partial h/\partial t$ with equation (2.10*a*) for the drainage-active region, which in terms of the non-mapped coordinates becomes

$$\dot{r}_D = -\left.\frac{\frac{1}{r}\frac{\partial}{\partial r}\left(rh^3\frac{\partial h}{\partial r}\right) - (\lambda h + 1)}{\partial h/\partial r}\right|_{r_D}. \tag{A 4b}$$

Second-order accuracy of the finite-difference representation of (A 4*b*) is achieved more easily in the non-mapped space than in the mapped space. In addition to the front evolution equations, two more boundary conditions are needed together with the four boundary conditions (2.10*b*)–(2.10*e*), to ensure continuity of thickness and flux at the joint interface, namely

$$[\![h]\!] = [\![q]\!] = 0 \quad \text{at } r = r_D. \tag{A 5}$$

We solve the evolution equations for the fronts and for the thickness in both domains simultaneously, using finite-volume discretization on a uniform grid and an implicit Crank–Nicolson scheme together with a predictor–corrector iteration to evaluate the nonlinear terms, and with adjustable time stepping. This scheme provides a second-order accuracy in both time and space for the solution of h and for the position of the two fronts. However, since $q \propto \partial h/\partial r$ the accuracy of solution for the flux is only first order. To compensate for the loss of accuracy we enhance the grid density.

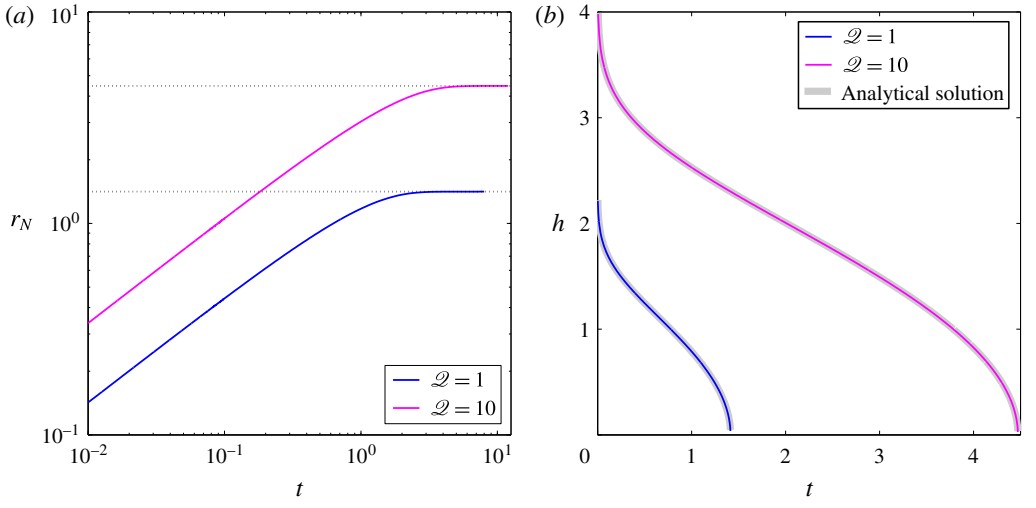

FIGURE 14. (Colour online) Comparison of the numerical solutions of the full equations with the analytic solution for the fully prewetted substrate (Spannuth *et al.* 2009). To simulate that situation we set $\lambda = 0$, $\mathscr{Q} = 1$ or 10 and $P = 1$, which prescribes the substrate to be permeable everywhere and sets the critical pressure to be zero. (*a*) The evolution of the fluid front r_N reaches a steady value equal to $\sqrt{2\mathscr{Q}}$ (grid lines), as the theory predicts. (*b*) The numerical solution of the thickness (– – – – blue, – – – – magenta), compared with the analytical solution of Spannuth *et al.* (2009) (– – – – grey).

We confirmed that the numerical solver is consistent with closed-form analytical solutions of several kinds: (i) propagation of a current on impermeable substrate ($P = 0$ everywhere; Huppert 1982), (ii) propagation of a current on a fully prewetted substrate ($P = 1$ everywhere; Spannuth *et al.* 2009) as shown in figure 14 and (iii) the late-time asymptotic flow in the permeable region (figure 2*a*).

REFERENCES

ACTON, J. M., HUPPERT, H. E. & WORSTER, M. G. 2001 Two-dimensional viscous gravity currents flowing over a deep porous medium. *J. Fluid Mech.* **440**, 359–380.

BEAR, J. 1988 *Dynamics of Fluids in Porous Media*. Dover Civil and Mechanical Engineering.

BOCZAR-KARAKIEWICZ, B., BONA, J. L. & PELCHAT, B. 1991 Interaction of internal waves with the seabed on continental shelves. *Cont. Shelf Res.* **11**, 1181–1197.

BOULANGE-PETERMANN, L., GABET, C. & BAROUX, B. 2006 Relation between the cleanability of bare or polysiloxane-coated stainless steels and their water contact angle hysteresis. *J. Adhes. Sci. Technol.* **20** (13), 1463–1474.

DAS, S. B., JOUGHIN, I., BEHN, M. D., HOWAT, I. M., KING, M. A., LIZARRALDE, D. & BHATIA, M. P. 2008 Fracture propagation to the base of the greenland ice sheet during supraglacial lake drainage. *Science* **320** (5877), 778–781.

DAVIS, S. H. & HOCKING, L. M. 1999 Spreading and imbibition of viscous liquid on a porous base. *Phys. Fluids* **11** (1), 48–57.

DAVIS, S. H. & HOCKING, L. M. 2000 Spreading and imbibition of viscous liquid on a porous base II. *Phys. Fluids* **12** (7), 1646–1655.

GROBELBAUER, H. P., FANNELOP, T. K. & BRITTER, R. E. 1993 The propagation of intrusion fronts of high-density ratios. *J. Fluid Mech.* **250**, 669–687.

HUPPERT, H. E. 1982 The propagation of two-dimensional and axisymmetric viscous gravity currents over a rigid horizontal surface. *J. Fluid Mech.* **121**, 43–58.

HUPPERT, H. E. 2006 Gravity currents: a personal perspective. *J. Fluid Mech.* **554**, 299–322.

HUPPERT, H. E. & NEUFELD, J. A. 2014 The fluid mechanics of carbon dioxide sequestration. *Annu. Rev. Fluid Mech.* **46** (1), 255–272.

HUPPERT, H. E. & WOODS, A. W. 1995 Gravity-driven flows in porous layers. *J. Fluid Mech.* **292**, 55–69.

LLEWELLIN, E. W., MADER, H. M. & WILSON, S. D. R. 2002 The rheology of a bubbly liquid. *Proc. R. Soc. Lond.* A **458** (2020), 987–1016.

MARINO, B. M. & THOMAS, L. P. 2002 Spreading of a gravity current over a permeable surface. *J. Hydraul. Engng* **128** (5), 527–533.

PIRAT, C., MATHIS, C., MAÏSSA, P. & GIL, L. 2004 Structures of a continuously fed two-dimensional viscous film under a destabilizing gravitational force. *Phys. Rev. Lett.* **92** (10), 104501.

PRITCHARD, D., WOODS, A. W. & HOGG, A. J. 2001 On the slow draining of a gravity current moving through a layered permeable medium. *J. Fluid Mech.* **444** (0), 23–47.

SIMPSON, J. E. 1999 *Gravity Currents: In the Environment and the Laboratory*. Cambridge University Press.

SPANNUTH, M. J., NEUFELD, J. A., WETTLAUFER, J. S. & WORSTER, M. G. 2009 Axisymmetric viscous gravity currents flowing over a porous medium. *J. Fluid Mech.* **622**, 135–144.

TADMOR, R. 2004 Line energy and the relation between advancing, receding, and young contact angles. *Langmuir* **20** (18), 7659–7664.

THOMAS, L. P., MARINO, B. M. & LINDEN, P. F. 1998 Gravity currents over porous substrates. *J. Fluid Mech.* **366** (0), 239–258.

THOMAS, L. P., MARINO, B. M. & LINDEN, P. F. 2004 Lock-release inertial gravity currents over a thick porous layer. *J. Fluid Mech.* **503**, 299–319.

UNGARISH, M. & HUPPERT, H. E. 2000 High-Reynolds-number gravity currents over a porous boundary: shallow-water solutions and box-model approximations. *J. Fluid Mech.* **418** (0), 1–23.

WOODS, A. W. & FARCAS, A. 2009 Capillary entry pressure and the leakage of gravity currents through a sloping layered permeable rock. *J. Fluid Mech.* **618**, 361–379.